Editors' Suggestion

Dynamic lift enhancement mechanism of dragonfly wing model by vortex-corrugation interaction

Yusuke Fujita and Makoto Iima*

Graduate School of Integrated Sciences for Life, Hiroshima University, 1-7-1, Kagamiyama, Higashi-Hiroshima, Hiroshima 739-8521, Japan

(Received 27 April 2023; accepted 16 October 2023; published 7 December 2023)

The wing structure of several insects, including dragonflies, is not smooth, but corrugated; its vertical cross section consists of a connected series of line segments. Some previous studies have reported that corrugated wings exhibit better aerodynamic performance than flat wings at low Reynolds numbers [Re $\simeq O(10^3)$]. However, the mechanism remains unclear because of the complex wing structure and flow characteristics. A corrugated structure modifies the formation and behavior of aerodynamic flow features arising during unsteady wing motion, such as the leading-edge vortex (LEV). These modifications can be key to lift enhancement in many insects, though the details of these benefits remain imperfectly understood. In this study, we analyzed the flow around a two-dimensional corrugated wing model that started impulsively by direct numerical simulations. We focused on the period between the initial generation of LEVs and subsequent interactions before detachment. For the flat wing, it is known that a secondary vortex with a sign opposite to that of the LEV, the λ vortex, develops and erupts to discourage lift enhancement. For corrugated wings, such an eruption of the λ vortex can be suppressed by the corrugation structure, which enhances the lift. The detailed mechanism and its dependence on the angle of attack are also discussed.

DOI: 10.1103/PhysRevFluids.8.123101

I. INTRODUCTION

Flying animals and vehicles vary significantly in their size and flow properties. The cord-based Reynolds number (Re) for a forward flight ranges from $O(10^0)$ (e.g., thrips) to $O(10^6)$ (e.g., passenger planes) [1]. As a result, the wing shapes also vary significantly. Typical wings of the high-Re flyers, such as passenger planes, have smooth surfaces because the surface roughness reduces the lift coefficients [2]. However, the wing surfaces of many insects such as dragonflies, cicadas, and bees are not smooth, and their Reynolds number is in the range of $O(10^2)$ to $O(10^4)$ (low-Re regime). Their wings are composed of nerves and membranes, and their cross-section shapes consist of vertices (nerves) and line segments (membranes). The geometry of the shape can be regarded as a connection of objects with a V shape or other shapes. This type of wing is known as a corrugated wing [3].

Aerodynamic studies on corrugated wings have contributed to their application in small flying robots, drones, and windmills, which are useful in the low-Re regime [4–8]. Because insects have low muscular strength, corrugated structures are expected to possess aerodynamic advantages [9].

We focused on the aerodynamic advantages of corrugated wings in the low-Re regime, wherein dynamic lift generation owing to flapping and the generation of leading-edge vortices are important, particularly for many insects, to achieve flight against their weight [1,10–15]. Other unsteady lift

*iima@hiroshima-u.ac.jp

enhancement mechanisms for insects have been reported, such as delayed (or absence of) stall, wake capture, and the clap-and-fling mechanism [12–14,16,17], wherein unsteady vortex generation due to flapping and its interaction with the wing play central roles. Most previous studies on unsteady lift enhancement mechanisms assumed a smooth wing. Our fundamental motivation was the effect of corrugation on such unsteady lift enhancement mechanisms. Previous studies on corrugated wings have not fully investigated this problem.

Many previous aerodynamic studies on corrugated wings focused on fixed wings in uniform flow at angles of attack (AoA) smaller than 20°, which may be related to the gliding flight [18–27]. The two mechanisms are described in the following two paragraphs.

The lift enhancement mechanism owing to the corrugated structure was discussed by Newman *et al.* [28] for $\mathrm{Re} = O(10^4)$, which is relatively high in this regime. They used a model wing with two parts: a corrugated part on the leading-edge side and a smoothed curved part on the trailing-edge side. They suggested that the V shapes in the corrugated wings acted as turbulators, provoking an early transition to turbulent flow to reduce the size of the separation bubble. This type of flow produces high lift [29]. Levy *et al.* [21] used the same model as Ref. [28] and performed two-dimensional numerical simulation at the smaller Re ($2000 \leqslant \mathrm{Re} \leqslant 8000$) to determine the vortex separations from the corrugations to reattach and reported a drag reduction and increased flight performance.

Vargas *et al.* [19] performed two-dimensional numerical simulation with one of the corrugated models taken from a dragonfly ("profile 2" in Ref. [30]) in a uniform flow at smaller AoA in the range $[0^\circ, 10^\circ]$, for $\mathrm{Re} < 10\,000$ and concluded that the aerodynamic performance of the corrugated wing model was equivalent to or better than that of the wing with the envelope of the corrugated wing (profiled wing). They also reported a trap of vortices in the valleys of the V shapes to make the overall flow resemble that around the profiled wings. Similar vortex traps have been observed in other experiments [31,32] and in two- and three-dimensional numerical simulations [26,27].

The following studies were performed for a corrugated wing model in a uniform flow with a wide range of AoA. Rees [31] used a hoverfly-based corrugated wing model, and measured its lift coefficient C_L and the drag coefficient C_D for $\mathrm{Re} = 450$, 800, and 900 over a range of AoA spanning from -22° to 50°. They reported that a corrugated wing yielded a larger C_L for $\mathrm{Re} = 800$ than the profiled wing. They also reported that the flow around the wing behaved as if the wing had an envelope profile. Kesel [30] used corrugated wing models based on the cross sections of a dragonfly wing for $\mathrm{Re} = 7800$ and $10\,000$ over a range of AoA spanning from -25° to 40°. The results show that C_L for the corrugated wing model is larger than that of the flat plate for some AoA.

Herein, we note that wings in unsteady motion can generate higher lifts at greater AoA. Dickinson *et al.* [11] analyzed impulsively started flat wings and reported higher lifts over time (the maximum lift was recorded at $\mathrm{AoA} = 45^\circ$). The leading-edge vortex (LEV) dynamics are particularly important [12]. An LEV is generated when a flat wing starts its translational motion from rest [1]. The LEV increases in size and circulation by feeding the vortex sheet separated from the leading edge [33,34]. During this process, a stagnation point on the upper surface of the wing, generated because of the flow toward the wing surface by the LEV, slides towards the trailing edge as the LEV moves toward the trailing edge with growth. Then, the direction of the flow on the wing surface between the stagnation point and the leading edge is reversed toward the leading edge, creating a secondary vortex of the opposite sign to the LEV, between the leading edge and the LEV. The shape of this secondary vortex resembles the greek character "λ" and is referred to as a λ vortex in this paper [1,35]. The LEV detaches from the wing after the stagnation point reaches its trailing edge. The λ vortex also grows and is responsible for detaching the LEV from the wing during eruptions [34,36]. After the LEV is released, the next LEV is generated.

In the case of corrugated wings, some studies have focused on dynamic performance. Luo and Sun [37] performed three-dimensional numerical simulations of revolving corrugated wing models. They concluded that the corrugated and flat wings exhibited almost the same performance. Bomphrey *et al.* [27] performed three-dimensional numerical simulations of a flapping wing. They reported that the pressure in the V-shaped region of the corrugated wing was lower and concluded that this low-pressure region was related to vortex formation in the V-shaped region and to the wide distribution of the negative-pressure area on the corrugated wing. However, vortex dynamics due to corrugation have not been fully examined. In particular, there are few studies on how the dynamics among vortices separated from the corrugation structures, LEV, and trailing-edge vortex work on the lift and drag production.

The theory of corrugated wings is also different from the steady-state aerodynamic theory which requires uniform flow and circulation of the wing alone (Kutta-Joukowski theorem) [38] and the unsteady-flapping flight mechanisms used by insects, such as delayed stall (LEV-wing interaction), rotation lift (circulation of wing owing to rotation), and wake capture (interaction among vortices generated from the edges). Unsteady flight mechanisms have been extensively studied [14,39]; however, corrugation alternates or modifies such mechanisms.

Real-life dragonflies flap their wings at high AoA during most flapping periods [40]. Thus, vortex dynamics among LEVs and other vortices are critical for aerodynamic performance. However, in the case of corrugated wings, it is challenging to determine whether the generated vortex motion is due to the wing structure or wing motion. Therefore, to discuss the dynamic aspects of the performance improvement of a corrugated wing, it is necessary to simplify the wing motion.

The purpose of this study was to understand the relationship between a corrugated wing structure and vortex motions. For this purpose, we considered a two-dimensional corrugated wing model. Furthermore, we simplified the wing motion and focused on unsteady lift generation by translating from rest. Translational motion is a principal component of wing motion, in addition to pitching and rotation [1,41]. This analysis expands our knowledge of the nonstationary mechanisms that dragonflies use during flight [11]. While our assumptions may exclude certain aspects of three-dimensionality and the complexity of real flapping motion, they still capture crucial vortex dynamics associated with corrugation. These dynamics include vortex generation from sharp corrugation edges, the leading edge, and the trailing edge. This aspect has been somewhat overlooked in previous research. The typical vortex interactions and lift generation discussed in this paper will prove valuable when investigating specific aspects of dragonfly wing structure and flapping motion. A similar approach has been applied to analyze flat wings [11,42–44]; however, this approach has not been performed intensively for corrugated wings. We previously investigated the aerodynamic properties of rapidly departing corrugated wings and found that λ-vortex collapse may improve the wing performance [35]. In the present study, we conducted a more detailed investigation. The corrugated wing exhibited a larger lift than the flat wing in the large-AoA regime. Moreover, the lift generation was closely related to the eruption of the λ vortex. The suppression of eruptions is key to evaluating and classifying dynamic lift enhancement.

The remainder of this paper is organized as follows. In Sec. II, the simulation method and its validation are discussed in detail. The results are presented and discussed in Sec. III. The lift-generation process is divided into two time periods. The vortex interaction stage, in which vortices grow sufficiently to detach and interact with each other, is discussed with a particular focus on the effect of the λ vortex. The results are summarized in Sec. IV.

II. METHOD

A. Corrugated wing model

A two-dimensional model of a corrugated wing was constructed using the real-life dragonfly wing (*Aeshna cyanea*) (Ref. [30], profile 1). The wing model was based on a cross section of the wing approximately 30% from the wing base. The structure of the model consists of deeper corrugated structures on their leading-edge side and less deep (flatter) structures on the trailing-edge side. This characteristic pattern shares its characteristics among real-life flying insects' corrugated wings.

The wing model was approximated using N line segments. The wing model was generated by adding thickness. We define the set of positions of the vertices and end points as $A = \{(x_k, y_k) \mid k =$

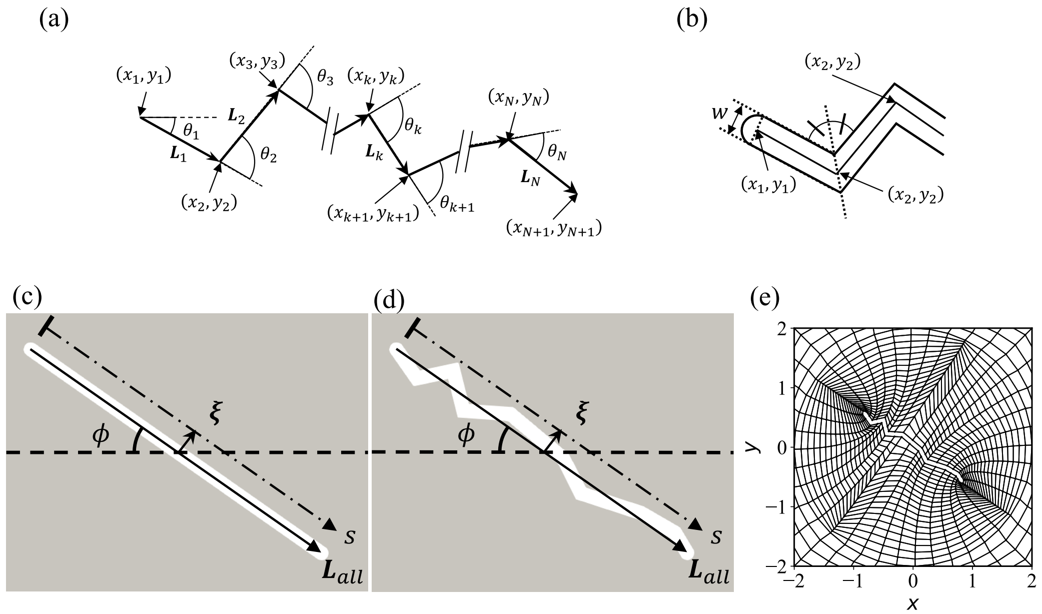

FIG. 1. Wing model descriptions. (a) Vertices (x_k, y_k), adjacent displacement vectors $\boldsymbol{L}_k$, and angles θ_k. (b) Line segments and thickness w of the wing model. (c) Flat wing model ($\alpha = 0$). (d) Corrugated wing model ($\alpha = 1$). (e) Spectral elements around corrugated wing model ($\phi = 35^\circ$).

$1, \ldots, N + 1\}$ [Fig. 1(a)]. Subsequently, a set of displacement vectors is defined as $B = \{\boldsymbol{L}_k \mid \boldsymbol{L}_k = (x_{k+1} - x_k, y_{k+1} - y_k); k = 1, \ldots, N\}$. The core shape of the corrugated wing model is determined using the set C consisting of the line segment lengths and angles between adjacent displacement vectors, that is, $C = \{L_k \mid L_k = |\boldsymbol{L}_k|; k = 1, \ldots, N\} \cap \{\theta_{k+1} \mid \theta_{k+1} = \cos^{-1}[\langle \boldsymbol{L}_k, \boldsymbol{L}_{k+1}\rangle/(L_k L_{k+1})]; k = 1, \ldots, N-1\}$, where $\langle \boldsymbol{a}, \boldsymbol{b}\rangle$ is the inner product of the vectors $\boldsymbol{a}$ and $\boldsymbol{b}$. We defined θ_1 as the angle between the x axis and $\boldsymbol{L}_1$ [Fig. 1(a)].

After the set C is determined, a family of corrugated wing shapes is characterized by introducing a shape parameter α; the shape is obtained by replacing θ_k with $\alpha\theta_k$ in the set C. In this study, we analyzed two cases, $\alpha = 0$ and 1, which corresponded to a flat plate wing (flat wing) and corrugated wing, respectively.

The core shape of the corrugated wing model was rescaled isotropically, such that the wing chord length c is 2, where $c = |\boldsymbol{L}_{\rm all}|$, and $\boldsymbol{L}_{\rm all} = \sum_{k=1}^{N} \boldsymbol{L}_k$. We note that the rescaling does not change the shape of the corrugation pattern. The thickness w of the wing was determined such that the relative thickness w/c is 0.04. Both ends of the wing core were semicircular [Fig. 1(b)]. Figures 1(c) and 1(d) show the wing models for $\alpha = 0$ and 1, respectively. The AoA ϕ is defined as the angle between $\boldsymbol{L}_{\rm all}$ and the x axis, which is parallel to the uniform flow, as shown in Figs. 1(c) and 1(d).

We also discuss the time variations in the pressure and vorticity distributions in a region near the upper surface. This region is characterized by a distribution along the line segment, which is a shifted vector of $\boldsymbol{L}_{\rm all}$ by $\boldsymbol{\xi}$, where $\boldsymbol{\xi} \perp \boldsymbol{L}_{\rm all}$ [Figs. 1(c) and 1(d)]. The position on the line segment is defined by s ($0 \leqslant s \leqslant 2$); $s = 0$ and 2 correspond to the leading and trailing edges when $\boldsymbol{\xi} = (0, 0)$, respectively. The amount of shift $|\boldsymbol{\xi}|$ and s are nondimensionalized by the wing chord length, that is, $\xi^* = \frac{|\boldsymbol{\xi}|}{c}$, $s^* = \frac{s}{c}$. According to our definition, $\xi^* = 0.02$ coincides with the upper surface of the flat wing model ($\alpha = 0$).

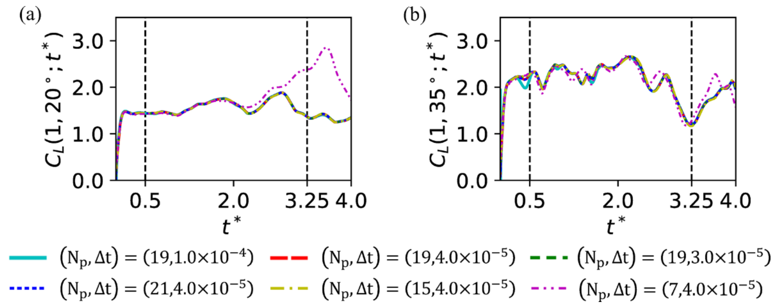

FIG. 2. Convergence of calculations for corrugated wing ($\alpha = 1$): (a) $C_L(1, 20^\circ; t^*)$ and (b) $C_L(1, 35^\circ; t^*)$.

B. Numerical simulation

The dimensionless two-dimensional incompressible Navier-Stokes equations

$$\frac{\partial \boldsymbol{u}}{\partial t} + (\boldsymbol{u} \cdot \nabla)\boldsymbol{u} = \frac{1}{\rho}\nabla p + \nu \Delta \boldsymbol{u}, \quad \nabla \cdot \boldsymbol{u} = 0, \tag{1}$$

were used to calculate the flow, where $\boldsymbol{u} = (u, v)$ is the velocity, p is the pressure, ρ is the air density, and ν is the kinematic viscosity. For the numerical calculations, we used the spectral element method, in which the computational domain was divided into a set of elements, and the physical quantities in each element were independently represented by a polynomial function with C^0 continuity across element boundaries [45]. As a result, the spectral element method balanced the exponential (spectral) convergence of errors associated with global collocation methods such as pseudospectral methods with the geometric flexibility of traditional low-order finite element methods [46]. The computational solver *Semtex* [46] was used to calculate Eq. (1). The computational domain was $[-30, 30] \times [-30, 30]$, and the center of the wing model was placed at (0,0) [Fig. 1(c)].

The boundary conditions of the outer sides of the computational domain, except for the right side ($x = 30, -30 \leqslant y \leqslant 30$), were set as the inflow, with $\boldsymbol{u} = \boldsymbol{U}(t^*)$, where $\boldsymbol{U}(t^*) = (0, 0)$ $(t^* < 0)$ and $\boldsymbol{U}(t^*) = (0, 0)$ $(t^* > 0)$. We note that the acceleration of flow is infinite at $t^* = 0$. The robust outflow conditions proposed in Ref. [47] with a smoothness parameter of 0.1 were applied to the right side. In this study, we set $\nu = 5 \times 10^{-4}$ such that the Reynolds number was Re $= 4000$, based on the chord length c. At the Reynolds number Re $= 1500, 4000$, the qualitative trends remain the same [35]. We set $\rho = 1$, but the value of ρ does not give any differences on the nondimensionalized results. The time step Δt was set to 4.0×10^{-5}, and the calculations were performed in the range $0 \leqslant t^* \leqslant 4$, where t^* is dimensionless time, $t^* = |\boldsymbol{U}|t/c$.

Figure 1(e) shows the spectral elements around the corrugated wing model ($\phi = 35^\circ$). The total number of spectral elements, N, was 2960, and each spectral element was discretized by $N_p \times N_p$ meshes [46]. Therefore, N_p is the number of points along the edge of each element. As N_p increases, the total number of meshes increases.

The calculations were verified for the corrugated wing model ($\alpha = 1$) at $\phi = 20^\circ$ and 35°. The time series of the lift coefficient $C_L(\alpha, \phi, t^*) = L/[(1/2)\rho c|\boldsymbol{U}|^2]$, where L represents the lift, is shown in Figs. 2(a) and 2(b). A convergence is demonstrated for N_p with values of 7, 15, 19, and 21 using $\Delta t = 4.0 \times 10^5$. Similarly, convergence is observed for Δt with values of 1.0×10^{-4}, 4.0×10^{-4}, and 3.0×10^{-4} when $N_p = 19$. The time-series data obtained with higher values of N_p and smaller Δt exhibited good agreement with each other.

To characterize the time ranges, we defined the maximum and mean lift coefficients in the time interval $[a, b]$, $C_{L,\max}(\alpha, \phi)$ and $C_{L,\text{mean}}(\alpha, \phi)$, respectively, as follows:

$$C_{L,\max}(\alpha, \phi) = \max_{a \leqslant t \leqslant b} C_L(\alpha, \phi; t), \quad C_{L,\text{mean}}(\alpha, \phi) = \frac{1}{b-a}\int_a^b C_L(\alpha, \phi; t)dt, \tag{2}$$

TABLE I. Convergence of C_L and $C_{L,\mathrm{mean}}$ for the corrugated wing ($\alpha = 1$) when $\Delta t = 4.0 \times 10^{-5}$.

	$\phi = 20^\circ$		$\phi = 35^\circ$	
N_p	$C_{L,\mathrm{mean}}$	$\lVert C_L(1,\phi)\rVert^{(N_p,21)}$	$C_{L,\mathrm{mean}}$	$\lVert C_L(1,\phi)\rVert^{(N_p,21)}$
21	1.5880	–	2.2147	–
19	1.5877	5.595×10^{-4}	2.2151	2.809×10^{-3}
15	1.5869	3.059×10^{-3}	2.2173	1.591×10^{-2}
7	1.7128	1.443×10^{-1}	2.1901	9.703×10^{-2}

and similar definitions for $C_{D,\mathrm{mean}}$. The relative difference in $C_{L,\max}$ between the corrugated wing and the flat wing, $\Delta_{\max}$, is defined as follows:

$$\Delta_{\max}(\phi) = \frac{C_{L,\max}(1,\phi) - C_{L,\max}(0,\phi)}{C_{L,\max}(0,\phi)}, \tag{3}$$

and similar definition for $\Delta_{\mathrm{mean}}(\phi)$.

These values were used to characterize the aerodynamic wing performance, and we discussed the relationship between these values and the flow field, that is, the pressure field, vorticity field, and flow speed field. The pressure was evaluated using the pressure coefficient, $C_p = \frac{p-p_\infty}{(1/2)\rho c|\boldsymbol{U}|^2}$, where p is the pressure and p_∞ is the inflow pressure (at positions $x = -30$). The flow speed was normalized by a uniform flow, $u^* = \frac{|\boldsymbol{u}|}{|\boldsymbol{U}|}$, where $|\boldsymbol{u}|$ is the flow speed.

The quantitative verification of the time averages of C_L, $C_{L,\mathrm{mean}}$ [Eq. (2)] for the corrugated wing ($\alpha = 1$) is shown in Table I. Herein, the time interval $(a, b) = (0.5, 3.25)$, corresponding to the intervals in Sec. III, was chosen. The convergence of $C_L(1,\phi;t)$ for N_p was also quantitatively confirmed using the norm $\lVert A\rVert^{(N_1,N_2)} = \frac{1}{b-a}\int_a^b |A^{(N_1)}(t) - A^{(N_2)}(t)|dt$, $(a, b) = (0.5, 3.25)$, where $A^{(N)}$ represents the calculation under the condition $N_p = N$. The case $A = C_L(1,\phi)$ is listed in Table I. Clear convergence of C_L and $C_{L,\mathrm{mean}}$ is observed for N_p in both cases of $\phi = 20^\circ$ and 35°.

In the following sections, $(N_p, \Delta t) = (19, 4.0 \times 10^{-5})$ was used for all calculations.

Lastly, we compared our simulation scheme with the immersed boundary method [44] under the following conditions: $\alpha = 0$ (flag wing), $\phi = 30^\circ$ for two Reynolds numbers, $\mathrm{Re} = 500$ and 1000. We have taken the value of $C_{L,\max}$. In the case of $\mathrm{Re} = 1000$, $C_{L,\max} \simeq 2.28$ in Ref. [44] (scanned value) and $C_{L,\max} = 2.36$ in our calculation. For $\mathrm{Re} = 500$, $C_{L,\max} \simeq 2.26$ in Ref. [44] and $C_{L,\max} = 2.33$ in our calculation. Both values agree reasonably well.

III. RESULT

The aerodynamic wing performance was evaluated using the lift coefficient $C_L(\alpha,\phi,t^*)$ and drag coefficient $C_D(\alpha,\phi,t^*) = D/[(1/2)\rho c|\boldsymbol{U}|^2]$, where D is the drag. Figures 3(a) and 3(b) show $C_L(\alpha,\phi,t^*)$ in the range $20^\circ \leqslant \phi \leqslant 40^\circ$ for the flat wing ($\alpha = 0$) and corrugated ($\alpha = 1$) wing, respectively.

In the initial range ($0 < t^* \leqslant 0.50$), $C_L(\alpha,\phi,t^*)$ shows a rapid change owing to the singularity of motion over a short period [inset of Fig. 3(a)]. Subsequently, the growth of the vortex separated from the leading and trailing edges, as well as the vertices of the corrugated structure, is observed. The LEV on the corrugated wing leaves the first V-shaped region and begins its motion on the wing around $t^* = 0.5$. Figures 4(a) and 4(b) show the normalized vorticity fields of the flat and corrugated wings, respectively ($\phi = 35^\circ$ at $t^* = 0.50$). Herein, the vorticity $\omega_z = \partial v/\partial x - \partial u/\partial y$ was normalized as $\omega_z^* = \frac{\omega_z c}{|\boldsymbol{U}|}$.

In the vortex interaction range ($0.50 < t^* < 3.25$), $C_L(\alpha,\phi,t^*)$ exhibited irregular oscillations for the corrugated wing ($\alpha = 1$). This range corresponded to the development of the LEV and secondary vortices generated on the upper wing surface, including vortex breakups and interactions

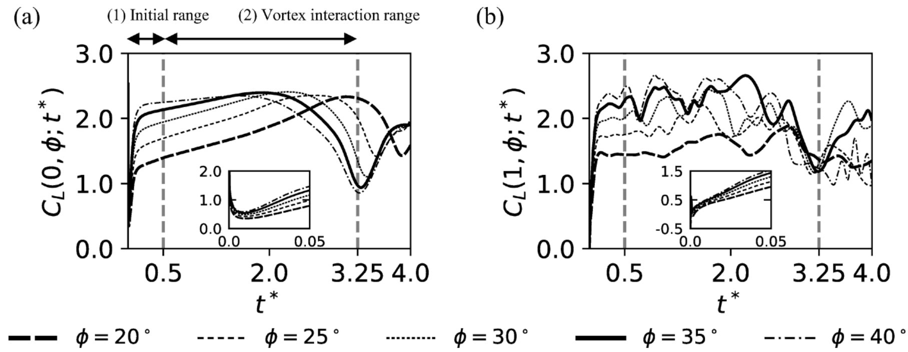

FIG. 3. Time series of the lift coefficient, $C_L(\alpha, \phi; t^*)$ ($20^\circ < \phi < 40^\circ$). (a) Flat wing ($\alpha = 0$). (b) Corrugated wing ($\alpha = 1$).

among the vortices, before leaving the vortices in the vicinity of the wing. The end of the range was determined by a decrease in $C_L(\alpha, 35^\circ, t^*)$ [Fig. 3 and Figs. 4(c) and 4(d)]; however, this range included the maximum lift time for the other cases during computation. We did not extend the range beyond this, as we were interested in the transient effects before the eventual limit cycle.

The major developments and interactions of the vortices were observed in the vortex interaction range ($0.50 < t^* < 3.25$). Therefore, in the following $(a, b) = (0.5, 3.25)$ in Eqs. (2). When b is fixed to 3.25, there are no qualitative dependencies on a in the range $0.02 \leqslant a \leqslant 1.1$. When a is

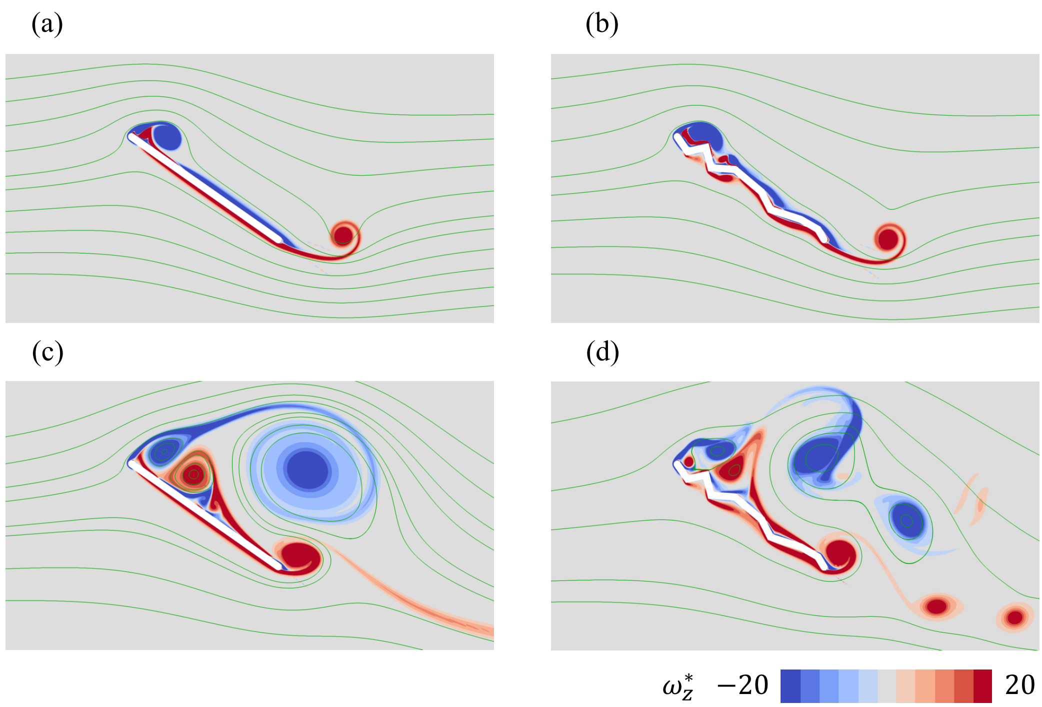

FIG. 4. Normalized vorticity fields for (a) a flat wing ($\alpha = 0$) for $\phi = 35^\circ$ at $t^* = 0.50$, (b) a corrugated wing ($\alpha = 1$) for $\phi = 35^\circ$ at $t^* = 0.50$, (c) a flat wing ($\alpha = 0$) for $\phi = 35^\circ$ at $t^* = 3.25$, and (d) a corrugated wing ($\alpha = 1$) for $\phi = 35^\circ$ at $t^* = 3.25$.

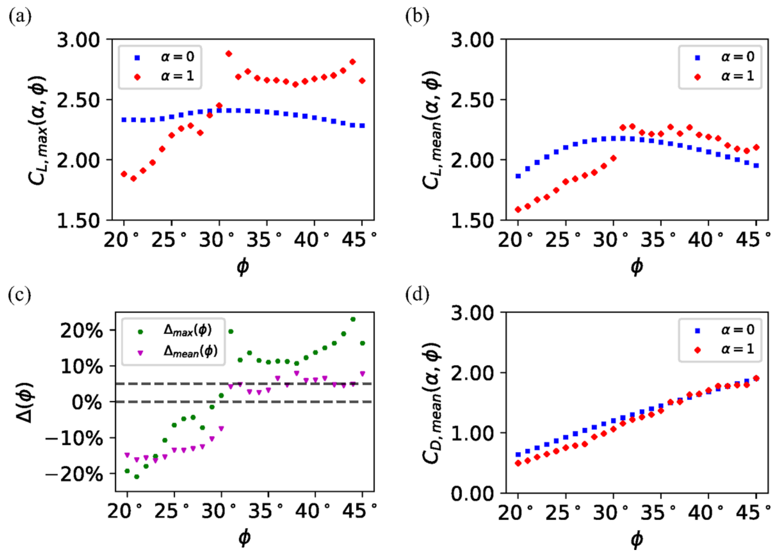

FIG. 5. (a) $C_{L,\max}$ during $0.5 < t^* < 3.25$ for the flat wing (blue, $\alpha = 0$) and corrugated wing (red, $\alpha = 1$). (b) $C_{L,\text{mean}}$ during $0.5 < t^* < 3.25$ for the flat wing (blue, $\alpha = 0$) and corrugated wing (red, $\alpha = 1$). (c) $\Delta_{\max}$ and Δ_{mean} during $0.5 < t^* < 3.25$. Vertical axis is in a percentage form. The dashed lines indicate 0% and 5%. (d) $C_{D,\text{mean}}$ during $0.5 < t^* < 3.25$ for the flat wing (blue, $\alpha = 0$) and corrugated wing (red, $\alpha = 1$).

fixed to 0.5, there is also no significant dependence on b in the range $2.5 \leqslant b \leqslant 4.0$. Thus, the results presented below are not sensitive to the detailed selection of the time interval.

A. Wing performance

Figures 5(a) and 5(b) show that the values of $C_{L,\max}$ and $C_{L,\text{mean}}$ for the corrugated wing are smaller than those of the flat wing when $\phi < 30^\circ$. However, the values of $C_{L,\max}$ and $C_{L,\text{mean}}$ for the corrugated wing are larger than those of the flat wing when $\phi > 30^\circ$. These graphs suggest that the lift coefficients of the corrugated and flat wings interchange at a critical value $\phi \simeq 30^\circ$. In particular, the performance of the corrugated wing clearly improves when $30^\circ < \phi$ ($\leqslant 45^\circ$); the mean value of $\Delta_{\max}$ over this range is 0.14 and the mean value of Δ_{mean} over this range is 0.05. Because the mean value of Δ_{mean} over the deteriorated case ($20^\circ \leqslant$) $\phi < 30^\circ$ was -0.14, the improvement between these cases is 22.1% ($\frac{1+0.05}{1-0.14} = 122.09$).

In Fig. 5(d), $C_{D,\text{mean}}$ is plotted against ϕ. No clear transitions are observed. When $\phi > 35^\circ$, the values of $C_{D,\text{mean}}$ for the corrugated and flat wings are almost the same, whereas $C_{D,\text{mean}}$ for the corrugated wing is smaller than that for the flat plate wing at $\phi < 35^\circ$. Therefore, the qualitative tendency of the lift-to-drag ratio L/D is similar to that of C_L. Therefore, we discuss C_L as wing performance hereafter.

The sign of $\Delta_{\max}$ and Δ_{mean} can be related to the pressure fields above the wing, as discussed below. Figure 6 shows the spatiotemporal distributions of the pressure on (t^*, s^*) ($0 \leqslant t^* \leqslant 4$, $0 \leqslant s^* \leqslant 1$) for $\xi^* = 0.15$. The parameter $\xi^* = 0.15$ is chosen as a position where the vortex motion can be observed well without interfering with the model. The leftmost column shows the distributions of the flat wing cases in $\phi = 20^\circ, 25^\circ, 30^\circ, 35^\circ$, and 40°. The five columns on the right show the distributions for the corrugated wing in $20^\circ \leqslant \phi \leqslant 44^\circ$.

When wing performance is improved ($30^\circ \leqslant \phi$; cf. Fig. 6), low-pressure regions appear near the leading-edge side periodically with a period of about 0.6. Such periodic regions are absent in corrugated wings without improved wing performance and in flat wings. Additionally, low-pressure

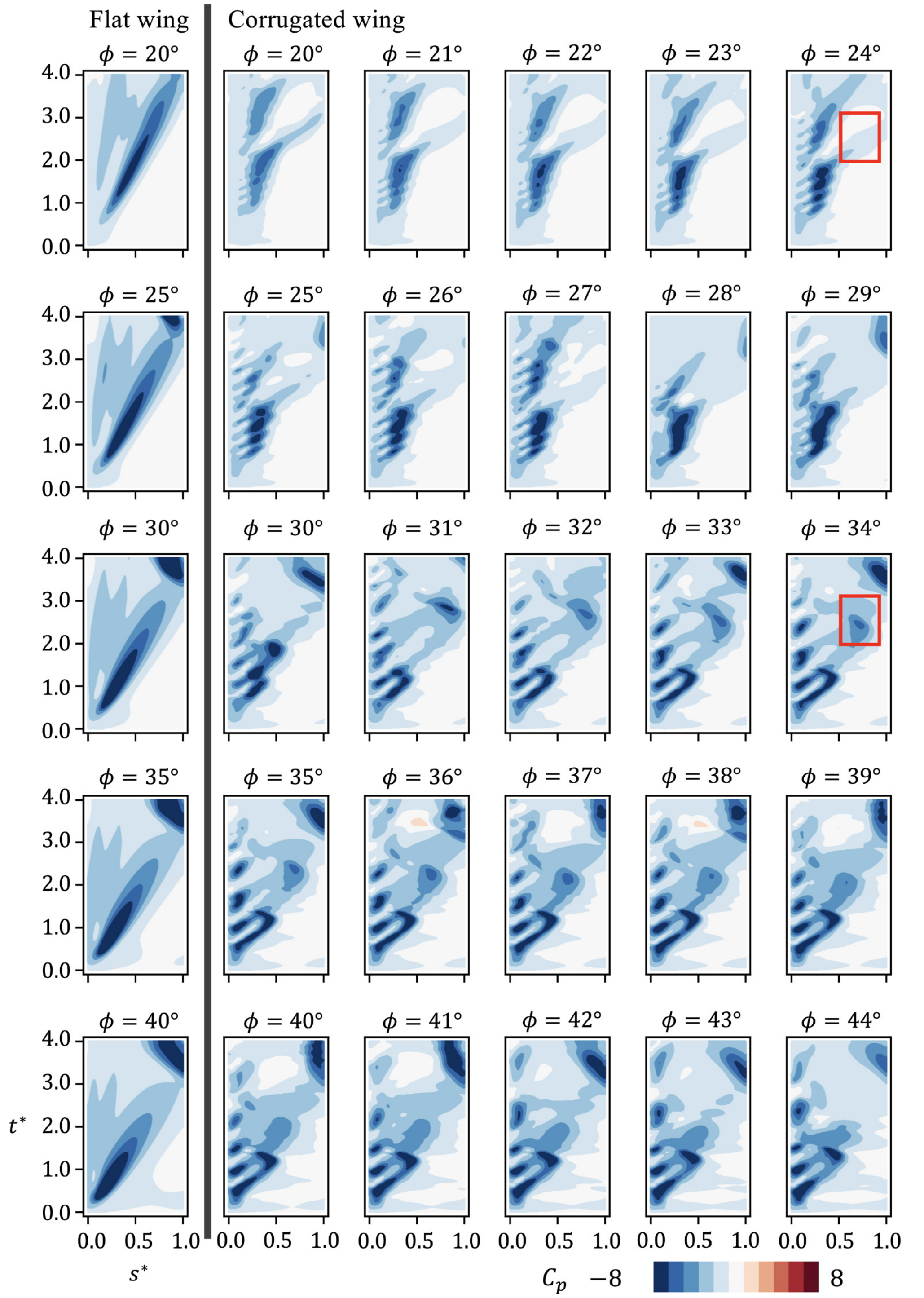

FIG. 6. Spatiotemporal distributions of C_p. $\xi^* = 0.15$. s^* axis and t^* axis are the horizontal and vertical axes, respectively.

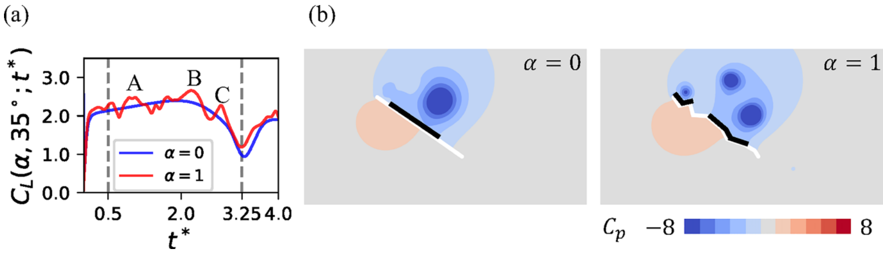

FIG. 7. (a) Time series of lift coefficient (blue, flat wing ($\alpha = 0$); red, corrugated wing ($\alpha = 1$); $\phi = 35°$). (b) Snapshots of the pressure field around the wings at $t^* = t^*_{\max}$.

regions appear periodically on the trailing-edge side ($0.5 \leqslant s^*$) during $2 < t^* < 3.25$. This trend is also observed for $\xi^* = 0.2$ (data not shown); it is insensitive to ξ^*.

B. Lift enhancement case: Instantaneous pressure and flow field

We selected the case $\phi = 35°$ as the typical case for the improvement of corrugated wing performance because the values of $C_{L,\max}$, and $C_{L,\text{mean}}$ were similar for $33° \leqslant \phi \leqslant 43°$ [Figs. 5(a) and 5(b)]. Therefore, the vortex dynamics described below can be considered a typical mechanism of dynamic lift enhancement.

Figure 7(a) shows the lift coefficients $C_L(\alpha, 35°; t^*)$ for the flat wing ($\alpha = 0$) and corrugated wing ($\alpha = 1$). A single maximum is recorded at $t^* \simeq 1.89$ for the flat wing, whereas multiple maxima are recorded for the corrugated wing owing to an oscillation around the curve of $C_L(0, 35°; t^*)$ [Fig. 7(a)]. The oscillations of $C_L(1, 35°; t^*)$ suggest a complex interaction between the vortices and the wing. For the following discussion, three major maxima, A, B, and C, are designated for $C_L(1, 35°; t^*)$. $t^*_{\max}$ is defined as the time that yields the greatest value of $C_L(\alpha, 35°; t^*)$, $t^*_{\max} = 1.89$ for the flat wing ($\alpha = 0$), and $t^*_{\max} = 2.21$ for the corrugated wing ($\alpha = 1$ corresponding to maximum B).

Figure 7(b) shows the pressure fields at $t^* = t^*_{\max}$. On the upper surface of the wing, the low-pressure regions of the corrugated wing are distributed over a wider range than those of the flat wing (regions where $C_p \leqslant -\frac{24}{11}$ are indicated by thick black lines). On the lower surface of the wing, the corrugated wing has a wider high-pressure region than the flat wing, which is similar to the initial range. Similar pressure distributions were observed at maxima A and C (data not shown).

C. Vortex dynamics of lift generation: Role of the λ vortex

The key vortex dynamics for the improving wing performance is as follows. Figure 8(a) shows the vorticity fields around a flat wing ($\alpha = 0$). Two snapshots at $t = 1.00$ and 1.70 are selected to explain the vortex dynamics before $t = t_{\max}$. At $t = 1.00$, two vortices with negative signs were formed from the leading edge (labeled 1 and 2), and a secondary vortex with a positive sign was sandwiched between them, as indicated by the arrow. The secondary vortex is called a λ vortex [1,11,34].

Vortex 1 continues to grow by feeding a vorticity-containing mass [34] as the value of C_L continues to increase until C_L records the maximum. During this period, these three vortices develop without changing their relative configurations, moving the center of vortex 1 away from the wing. Concurrently, the stagnation point owing to the flow pushing on the surface of the wing slides downstream to approximately reach the trailing edge. This result is consistent with those of previous studies [1,34]. In terms of pressure, the low-pressure region at the center of vortex 1 moved away from the wing. Consequently, the lift-generation process is monotonic, and the (local) maximum occurs only once in the vortex interaction range.

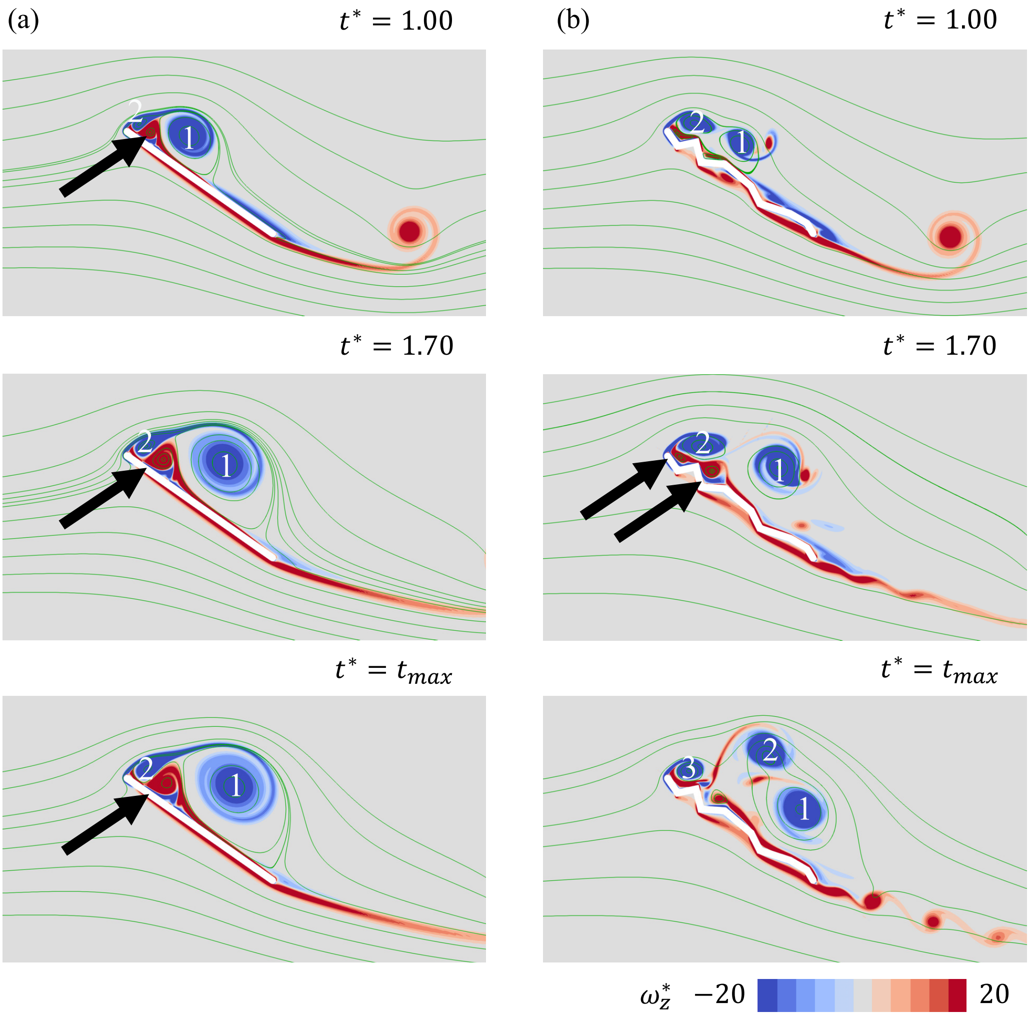

FIG. 8. Snapshots of the normalized vorticity fields ($\phi = 35°$) for (a) the flat plate wing ($t^* = 1.00$, $t^* = 1.70$, and $t^* = t_{\max}$) and (b) the corrugated wing ($t^* = 1.00$, $t^* = 1.70$, and $t^* = t_{\max}$).

However, the behavior of the λ vortex on the corrugated wing is significantly different from that of the flat wing because of the irregular surface structure; that is, the λ vortex collapses, splits into several smaller vortices owing to the corrugated structures, and gets stuck in the V-shaped regions of the wing [Fig. 8(b), $t^* = 1.70$, indicated by arrows]. Consequently, the λ vortex behavior replaces the unsteady vortex dynamics that characterize insect flight mechanisms, as described below.

Figure 8(b) shows the vorticity field around the corrugated wing ($\alpha = 1$). At $t^* = 1.00$, two vortices with negative signs are formed near the leading edge (labeled 1 and 2). These vortices were originally separated from the leading edge as in the case of a flat wing ($\alpha = 0$). Here, vortex 1 is detached from the vortex sheet connected to the leading edge, as is vortex 2 soon after $t^* = 1.70$. Therefore, vortices 1 and 2 act as independent vortices, which is a major difference from the case of the flat wing. Consequently, the relative positions of the vortices at $t^* = t_{\max}$ are significantly different from that in the case of the flat wing [Fig. 8(b)].

Consequently, vortex 2, which is nearest to vortex 1, advects vortex 1 downward to the wing surface. Unlike in the case of the flat wing, the λ vortex does not contribute to the motion of vortex

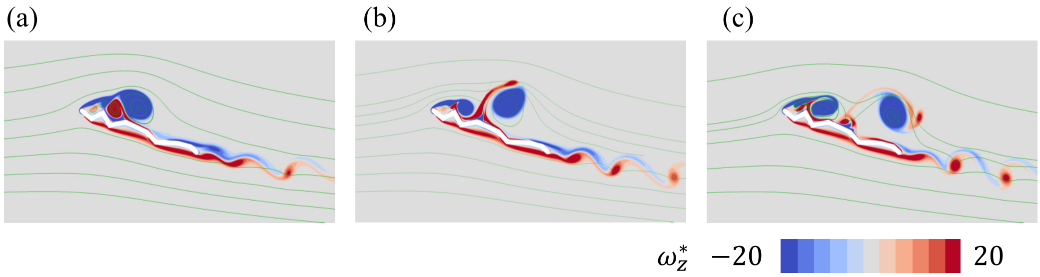

FIG. 9. Typical snapshots of the normalized vorticity fields around the corrugated wing ($\alpha = 1, \phi = 20^\circ$): (a) $t^* = 2.15$, (b) $t^* = 2.45$, and (c) $t^* = 2.81 = t^*_{\max}$.

1 owing to the collapse. The proximity of vortex 1 results in a wider high-pressure region at $t^* = t^*_{\max}$ (maximum B) [Fig. 8(b); cf. Fig. 7(b) for the pressure field].

We selected the case $\phi = 20^\circ$ as the typical case for the nonimprovement of corrugated wing performance because the values of Δ_{mean} were similar for $20^\circ \leqslant \phi \leqslant 28^\circ$ [Fig. 5(c)]. Snapshots of the vorticity field, in this case, are compared with the case $\phi = 35^\circ$ (Fig. 8), where wing performance is improved. When wing performance is not improved ($\phi \leqslant 30^\circ$), the λ vortex grows on the upper surface of the wing [Fig. 9(a)]. The λ vortex then stretches to interfere with the larger LEV, preventing it from being pulled to the wing [Figs. 9(b) and 9(c)].

In both cases, with and without an improvement in the performance of the corrugated wing, the vortex dynamics explained above were common. Figure 10 shows the spatiotemporal distribution of vorticity on (t^*, s^*) $(0 \leqslant t^* \leqslant 4,\ 0 \leqslant s^* \leqslant 1)$ for $\xi^* = 0.15$. The leftmost column shows the distributions for the flat wing cases at $\phi = 20^\circ, 25^\circ, 30^\circ, 35^\circ$, and 40°. The remaining five columns show the same for the corrugated wing at $20^\circ \leqslant \phi \leqslant 44^\circ$.

The eruption of the λ vortex corresponds to a positively signed vortex recorded near $t^* = 2$, $s^* = 0.25$ (cf. arrow in $\phi = 20^\circ$ in Fig. 10). Subsequently, the eruption causes the vortex to move toward the trailing edge with time (cf. Fig. 9). Therefore, the λ vortex expands from a certain time when viewed on the s^* axis, with vorticity of positive sign being recorded. In addition to this, because of the background flow, the vorticity of positive sign moves in a positive direction on the s^* axis over time. To quantify the vortex eruption, a vorticity field satisfying $s^* > 0.25$, $1.5 < t^* < 2.5$, and $\omega_z^* \geqslant 20$ was extracted to perform linear fitting using the least-squares method. For example, the extracted regions (magenta) and fitted lines for the corrugated wing at $\phi = 20^\circ$ and 35° are shown in Figs. 11(a) and 11(b), respectively. This method allowed detecting stretched vortices. The mean squared error (MSE) of the fitting and slope of the regression line are plotted in Fig. 11(c).

In the case of no improvement in the wing performance [Fig. 11(c), red circle], the slope is concentrated around 1 and the MSE is small and localized. This implies that the vortex with a positive sign moves to the trailing edge, corresponding to a λ vortex eruption. When the wing performance is improved [Fig. 11(c), green circles], the slope is small or the variation is large, and the result depends on ϕ. No clear λ-vortex eruption is identified.

For the flat wing [Fig. 11(c), blue cross], the slope is concentrated in a range larger than 1. This also indicates that a vortex with a positive sign has moved to the trailing edge in that region, corresponding to a λ-vortex eruption.

For corrugated wings with $30^\circ \leqslant \phi$, vortices with negative signs are periodically generated at the leading-edge side, as shown in Fig. 10. This corresponds to the pressure-field results shown in Fig. 6. This trend is also observed for $\xi^* = 0.1$; it is insensitive to ξ^*.

D. Mean behavior

In this section, we focus on the mean flow behavior to discuss the lift enhancement mechanism of the corrugated wing over the time interval of the vortex interaction range. We compared the

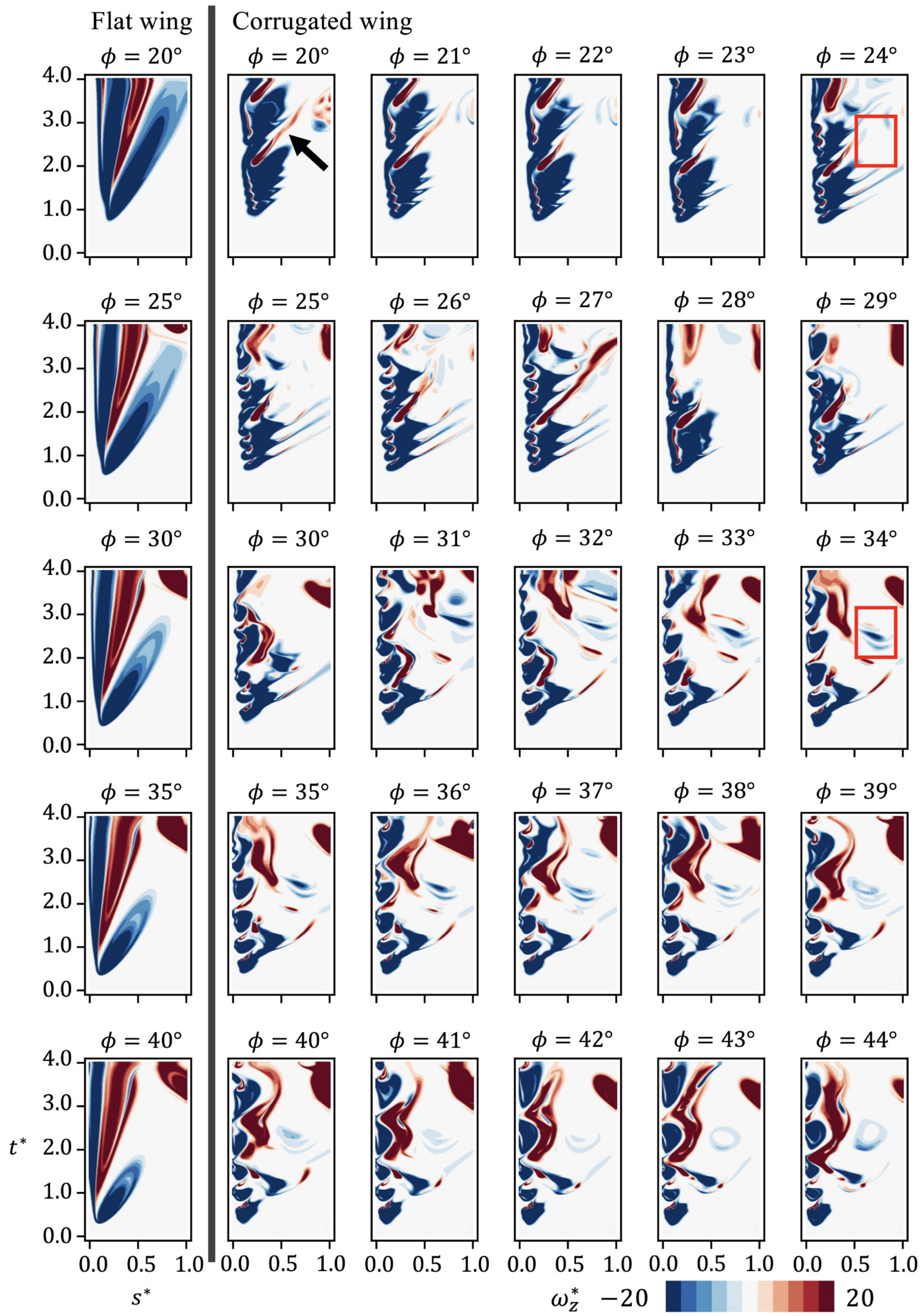

FIG. 10. Spatiotemporal distributions of the vorticity field. $\xi^* = 0.15$. s^* axis and t^* axis are the horizontal and vertical axes, respectively.

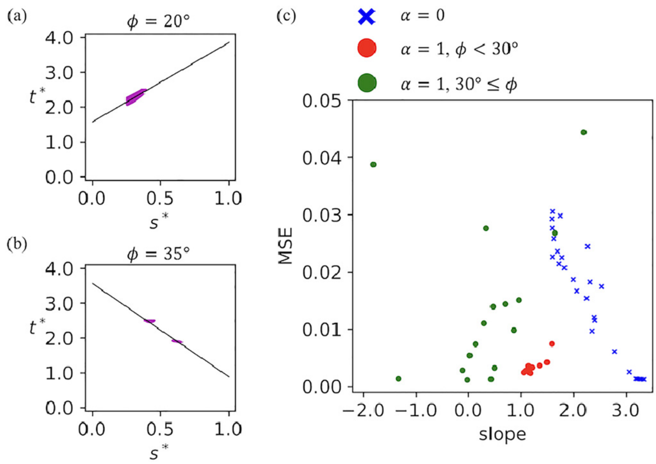

FIG. 11. Extraction of λ vortex eruptions. (a) The corrugated wing ($\alpha = 1, \phi = 20^\circ$). (b) The corrugated wing ($\alpha = 1, \phi = 35^\circ$). (c) Results of linear regression for the distribution of the λ vortex. Phase diagram of slope and mean squared error.

following two cases: $\phi = 35^\circ$ for the lift enhancement, and $\phi = 20^\circ$ when the lift is not enhanced. The mean pressure and vortex fields are shown in Fig. 12 (case $\phi = 35^\circ$) and Fig. 13 (case $\phi = 20^\circ$). For the discussion below, we define the following two regions: the region on the upper side near the leading edge (region 1) and that of the rest of the wing [region 2; insets of Figs. 12(b) and 13(b)]. Region 1 contains two V-shaped regions and the boundary is defined by (x_5, y_5).

We discuss the behaviors in regions 1 and 2 separately. In region 1, the negative-pressure region on the corrugated wing was wider than that on the flat plate when $\phi = 35^\circ$ [Figs. 12(a) and 12(b); for example, the region where $C_p \leqslant -\frac{24}{11}$]. This negative-pressure region corresponded to a round vortex region with a positive sign stuck in the V-shaped region [Fig. 12(d)], which was caused by the collapse of the λ vortex. The details are presented in Sec. III E. However, for the case $\phi = 20^\circ$, the negative-pressure distributions for both wings were similar in this region [Figs. 13(a) and 13(b)]. The stronger negative-pressure region (where $C_p \leqslant -\frac{24}{11}$) did not cover the wing surface [Fig. 13(b)] because the round vortex was smaller [Fig. 13(d), arrow].

In region 2, the pressure distributions on both wings were similar for $\phi = 35^\circ$ [Figs. 12(a) and 12(b)]. The vorticity distribution formed a round shape for the corrugated wing, and the LEV remained in this region for a certain time interval [Fig. 12(d)]. In contrast, the vorticity region for the flat plate wing was elongated as a result of LEV development in a similar manner [Fig. 12(c)].

As for $\phi = 20^\circ$, the negative-pressure region on the flat plate wing was wider than that on the corrugated wing [Figs. 13(a) and 13(b)], which was consistent with the fact that the value of Δ_{mean} was negative [cf. Fig. 5(c)]. For a corrugated wing, the round vorticity region observed in the case $\phi = 35^\circ$ shifted to the leading-edge side, and no distinct vorticity region was observed in this region [Fig. 13(d)], which explained the narrow negative-pressure region [Fig. 13(b)]. In contrast, the vorticity region for the flat plate was relatively close to the wing surface, and the negative-pressure region was maintained [Fig. 13(a)].

In summary, the mean lift enhancement was analyzed by focusing on these two regions. On the lower surface of the wing, the flow was almost steady and the "profiled wing" image was valid for all the investigated ϕs, although previous studies have been limited to smaller AoA [19,21]. However, on the upper surface, vortex dynamics played a decisive role in evaluating lift generation. When the corrugated wing generated a larger lift, the LEV remained near the wing, which required the elimination of interference by the λ vortex. The corrugation broke the λ vortex to become stuck in V-shaped regions. However, the detailed dynamics near the leading edge require further discussion, as discussed in the following section.

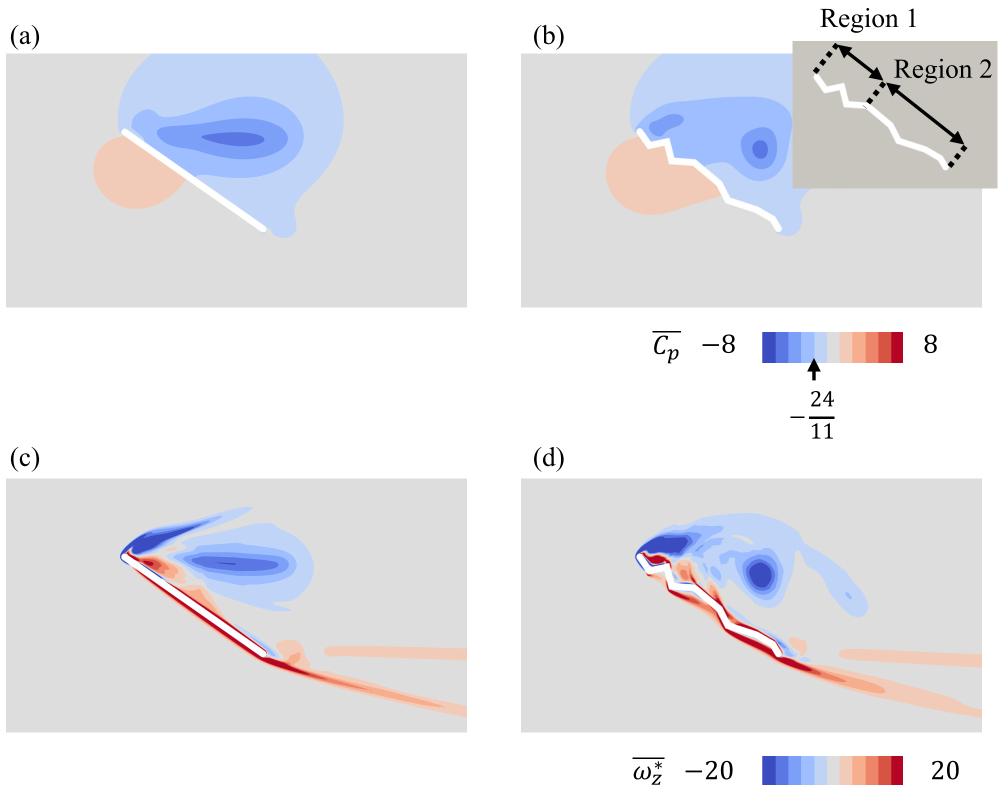

FIG. 12. Mean pressure fields around (a) the flat wing ($\alpha = 0$, $\phi = 35^\circ$) and (b) the corrugated wing ($\alpha = 1$, $\phi = 35^\circ$), and the definition of the region around the corrugated wing model for understanding the flow characteristics. Mean normalized vorticity fields around (c) the flat wing ($\alpha = 0$, $\phi = 35^\circ$) and (d) the corrugated wing ($\alpha = 1$, $\phi = 35^\circ$).

E. Vortex dynamics near the leading edge: How the low-pressure region is generated

In this section, we explain the generation of mean low pressure in the V-shaped region due to the λ vortex collapse and LEV in the corrugated wing [Fig. 12(b)].

Let us compare the position of the low-pressure region at $t = t^*_{\max}$ [Figs. 7(b) and 7(c)] and in the mean fields [Figs. 12(a) and 12(b)]. On the upper surface of the wing, the corrugated wing has a strong negative-pressure area in the first V-shaped region counted from the leading edge [Fig. 12(b)]. This low-pressure area does not form in the second V-shaped region [Fig. 12(a)]. However, for the flat wing, a strong negative-pressure area is present at a certain distance from the leading edge. In both cases, the negative-pressure region on the wing owing to the proximity of the vortex [as discussed in Sec. III B; Fig. 7(b)] did not appear in the mean field [Fig. 12(b)]. In contrast, the negative-pressure region in the first V-shaped region remains a snapshot when the maximum lift is recorded [Figs. 7(b) and 8].

Figure 14 shows the flow fields for a corrugated wing ($\alpha = 1$) at $t^* = 1.80$ and 2.15. These particular times are chosen to evaluate wing performance near the leading edge in terms of the mean flow field such that the two typical vortex dynamics explained below are clearly visible.

Figures 14(a) and 14(c) show the pressure and vorticity fields at $t^* = 1.80$, respectively. A vortex with a negative sign is formed from the leading edge, and a secondary vortex with a positive sign, generated by the collapse of the λ vortex, is formed between the wing and the vortex [Fig. 14(c), indicated by the arrow]. Accordingly, a negative-pressure region is formed in the first V-shaped region [Fig. 14(a), indicated by the arrow].

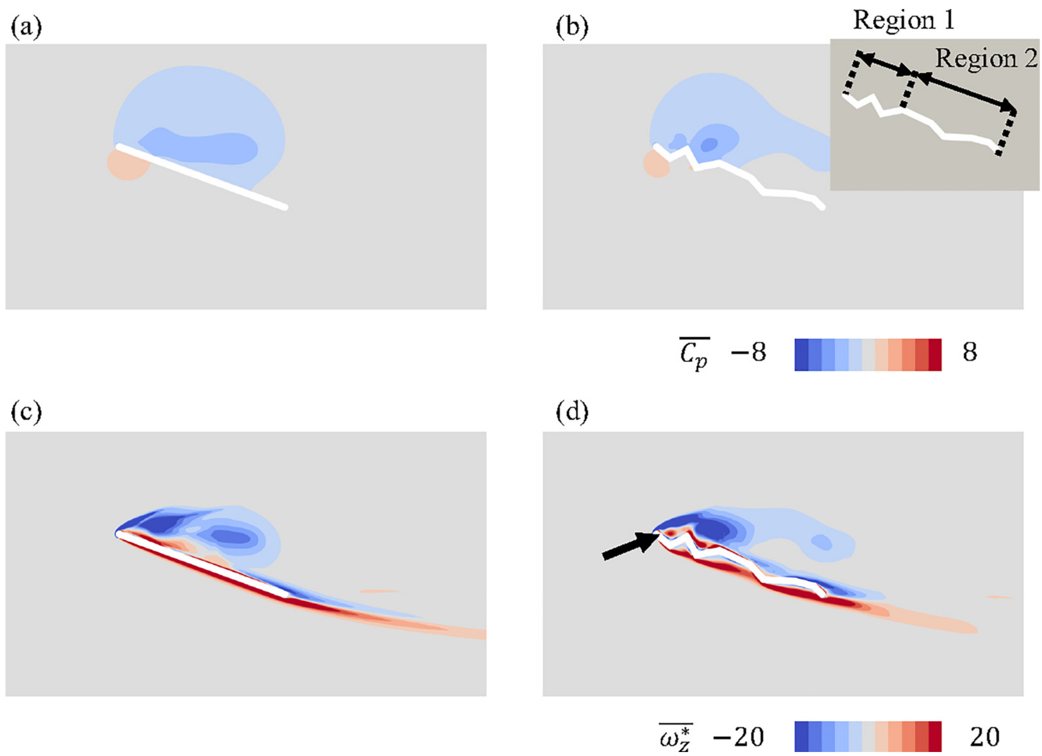

FIG. 13. Mean pressure fields around (a) the flat wing ($\alpha = 0$, $\phi = 20^\circ$) and (b) the corrugated wing ($\alpha = 1$, $\phi = 20^\circ$), and the definition of the region around the corrugated wing model for understanding the flow characteristics. Mean normalized vorticity fields around (c) the flat wing ($\alpha = 0$, $\phi = 20^\circ$) and (d) the corrugated wing ($\alpha = 1$, $\phi = 20^\circ$).

Figures 14(b) and 14(d) show the pressure and vorticity, respectively, at $t^* = 2.15$. Here, a vortex with a positive sign is squashed [Fig. 14(d)]. Accordingly, the squashed region corresponds to the low-speed region. A vortex with a positive sign in the leading-edge concavity forms a dead-water region and is transmitted, and the negative pressure created by the LEV acts on the wing surface [Fig. 14(b)].

As described above, the dynamics in the first V-shaped region is not stationary, but dynamic. Nonetheless, a mean low-pressure region is generated because both round vortices exhibit positive and negative signs, and they contribute to the low-pressure region. The periodic generation of vortices with both signs is also observed in Figs. 6 and 10. This process persists after time averaging, as shown in Fig. 12.

IV. CONCLUDING REMARKS

In this study, the flow around a two-dimensional corrugated wing was analyzed using direct numerical calculations at Re = 4000, and the wing performance was compared with that of a flat wing. The performance of the corrugated wing was better when the AoA was greater than 30°.

The uneven structure of the corrugated wing generates an unsteady lift owing to complex flow structures and vortex motions. Herein, we discuss several lift enhancement mechanisms owing to the uneven structure of a single corrugated wing model of a dragonfly.

The first is the pressure reduction on the upper side of the corrugated wing owing to the interactions of the vortices detached from the leading edge. The detachment and formation of vortices result from the collapse of the λ vortex.

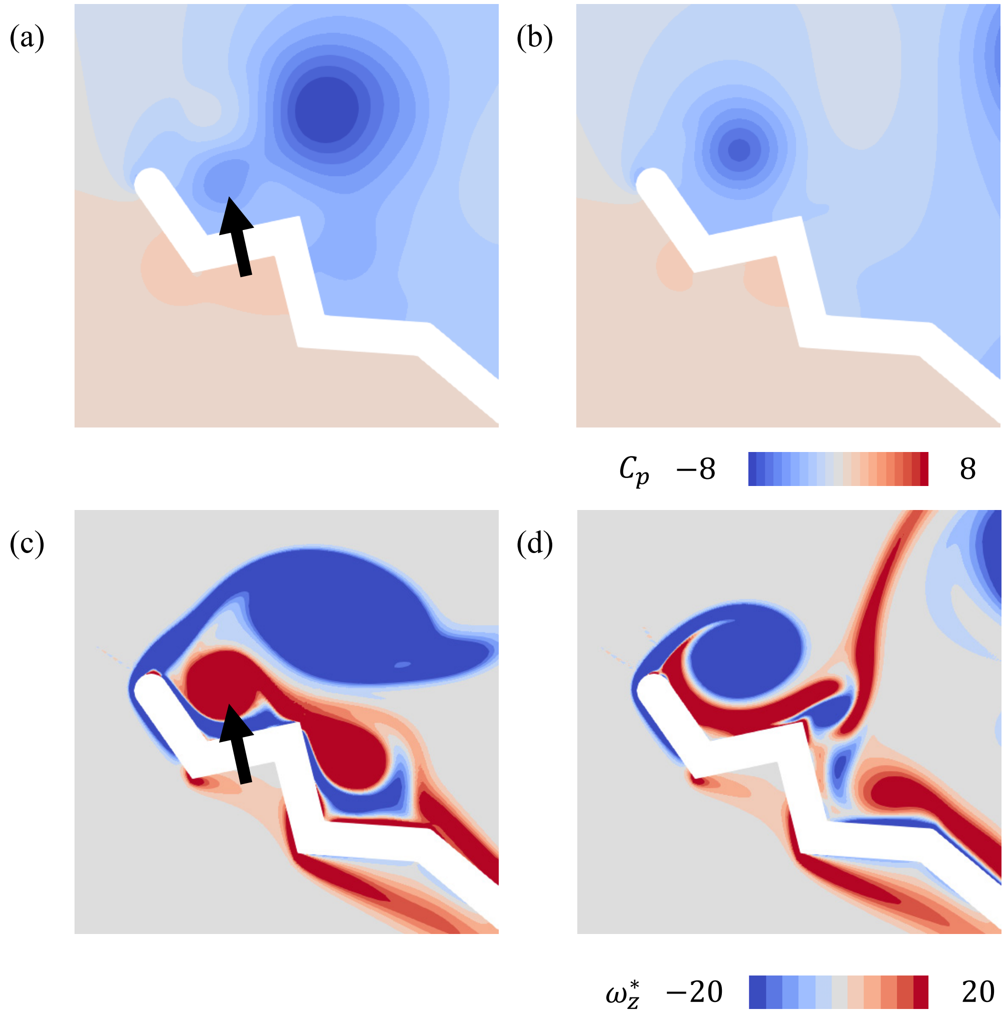

FIG. 14. Typical snapshots of the flow field near the leading edge of the corrugated wing ($\alpha = 1, \phi = 35°$). Pressure fields at (a) $t^* = 1.80$ and (b) $t^* = 2.15$. Vorticity fields at (c) $t^* = 1.80$ and (d) $t^* = 2.15$.

The second is the dynamic generation of a mean low-pressure region in the V-shaped structure near the leading edge on the upper side of the corrugated wing. Here, the collapsed λ vortices and LEV stuck in the V-shaped region near the leading edge form a negative-pressure region, thereby generating an averaged negative-pressure area. To the best of our knowledge, these mechanisms are dynamic and have not been reported elsewhere. However, the explanation of the detailed dynamics, including the period of the successive process, remains for a future work.

We have proposed some of the characteristic dynamics for the lift enhancement of the corrugated wing based on the simplified corrugated wing and wing motion, because in a realistic situation of dragonfly's flapping wing, both the wing-shape details and the vortex motion are too complex to understand. Our simplifications discard information intrinsic to the three-dimensionality, the detailed flapping motion. Nevertheless, we believe that the proposed dynamics will be useful when tackling more realistic models of a dragonfly's corrugated wing, because they are based on the fundamental dynamics related to the leading-edge vortex and uneven structures.

Such mechanisms can be used for novel wing shape designs, particularly in the low-Reynolds-number regime corresponding to insect flight. This is similar to the passive drag reduction of turbulent flow; the drag can be reduced by approximately 8% by simply changing the surface shape [48]. However, for further understanding, the relationship between wing shape and aerodynamic performance should be studied in more detail. These mechanisms are used to analyze various corrugation patterns and flows (for example, different Re). The authors also studied an inverted corrugated wing model to obtain similar results [35]. Additional details will be reported elsewhere.

Additionally, the dependence on the Reynolds number is important. We have reported that the qualitative trends remain broadly the same at Re = 1500 and 4000 [35]. However, as the Reynolds number decreases, the vortex motion may differ from that shown here because of the viscous effects. Further details will be reported elsewhere.

In this study, we considered two-dimensional models. However, this study focused on the aerodynamics of insect flight, in which the flow is typically three dimensional. If these results are expanded to a three-dimensional system, we expect to gain more practical knowledge for understanding insect flight and its application in the industry. Investigations in three-dimensional space will be the subject of future research. We can gain a clearer understanding by resolving these issues.

ACKNOWLEDGMENTS

This work was partially supported by Japan Society for the Promotion of Science KAKENHI Grant No. 19K03671, No. 21H05303, and No. 22KJ2316 and SECOM Science and Research Foundation.

[1] J. D. Eldredge and A. R. Jones, Leading-edge vortices: Mechanics and modeling, Annu. Rev. Fluid Mech. **51**, 75 (2019).
[2] I. H. Abbott and A. E. Von Doenhoff, *Theory of Wing Sections: Including a Summary of Airfoil Data* (Dover publications, New York, 1949).
[3] R. Dudley, *The Biomechanics of Insect Flight: Form, Function, Evolution* (Princeton University Press, Princeton, NJ, 2002).
[4] A. Obata, S. Shinohara, K. Akimoto, K. Suzuki, and M. Seki, Aerodynamic bio-mimetics of gliding dragonflies for ultra-light flying robot, Robotics **3**, 163 (2014).
[5] C. Wang, W. Zhang, Y. Zou, R. Meng, J. Zhao, and M. Wei, A sub-100 mg electromagnetically driven insect-inspired flapping-wing micro robot capable of liftoff and control torques modulation, J. Bionic Eng. **17**, 1085 (2020).
[6] L. T. K. Au, H. V. Phan, S. H. Park, and H. C. Park, Effect of corrugation on the aerodynamic performance of three-dimensional flapping wings, Aerosp. Sci. Technol. **105**, 106041 (2020).
[7] J. Chahl, N. Chitsaz, B. McIvor, T. Ogunwa, J.-M. Kok, T. McIntyre, and E. Abdullah, Biomimetic drones inspired by dragonflies will require a systems based approach and insights from biology, Drones **5**, 24 (2021).
[8] J. Holbert, A. Jacob, N. Peters, and Z. Sternberg, Vertical axis windmill, Am. J. Mech. Eng. **6**, 1 (2018).
[9] H. Tanaka and R. J. Wood, Fabrication of corrugated artificial insect wings using laser micromachined molds, J. Micromech. Microeng. **20**, 075008 (2010).
[10] C. P. Ellington, The aerodynamics of hovering insect flight. IV. Aerodynamic mechanisms, Philos. Trans. R. Soc. London, Ser. B **305**, 79 (1984).
[11] M. H. Dickinson and K. G. Götz, Unsteady aerodynamic performance of model wings at low Reynolds numbers, J. Exp. Biol. **174**, 45 (1993).
[12] C. P. Ellington, C. Van Den Berg, A. P. Willmott, and A. L. Thomas, Leading-edge vortices in insect flight, Nature (London) **384**, 626 (1996).
[13] S. P. Sane, The aerodynamics of insect flight, J. Exp. Biol. **206**, 4191 (2003).

[14] D. D. Chin and D. Lentink, Flapping wing aerodynamics: From insects to vertebrates, J. Exp. Biol. **219**, 920 (2016).

[15] W. Shyy, C.-k. Kang, P. Chirarattananon, S. Ravi, and H. Liu, Aerodynamics, sensing and control of insect-scale flapping-wing flight, Proc. R. Soc. A. **472**, 20150712 (2016).

[16] M. H. Dickinson, F.-O. Lehmann, and S. P. Sane, Wing rotation and the aerodynamic basis of insect flight, Science **284**, 1954 (1999).

[17] T. Weis-Fogh, Quick estimates of flight fitness in hovering animals, including novel mechanisms for lift production, J. Exp. Biol. **59**, 169 (1973).

[18] R. Buckholz, The functional role of wing corrugations in living systems, J. Fluids Eng. **108**, 93 (1986).

[19] A. Vargas, R. Mittal, and H. Dong, A computational study of the aerodynamic performance of a dragonfly wing section in gliding flight, Bioinspir. Biomim. **3**, 026004 (2008).

[20] H. Hu and M. Tamai, Bioinspired corrugated airfoil at low Reynolds numbers, J. Aircr. **45**, 2068 (2008).

[21] D.-E. Levy and A. Seifert, Simplified dragonfly airfoil aerodynamics at Reynolds numbers below 8000, Phys. Fluids **21**, 071901 (2009).

[22] D.-E. Levy and A. Seifert, Parameter study of simplified dragonfly airfoil geometry at Reynolds number of 6000, J. Theor. Biol. **266**, 691 (2010).

[23] S. F. Anwer, I. Ashraf, H. Mehdi, A. Ahmad, and H. Grafi, On the aerodynamic performance of dragonfly wing section in gliding mode, Adv. Aerosp. Sci. Appl. **3**, 227 (2013).

[24] X. G. Meng and M. Sun, Aerodynamic effects of wing corrugation at gliding flight at low Reynolds numbers, Phys. Fluids **25**, 071905 (2013).

[25] Z. Zhang, Y. Yin, Z. Zhong, and H. Zhao, Aerodynamic performance of dragonfly wing with well-designed corrugated section in gliding flight, Comput. Model. Eng. Sci. **109**, 285 (2015).

[26] M. I. Ansari, M. H. Siddique, A. Samad, and S. F. Anwer, On the optimal morphology and performance of a modeled dragonfly airfoil in gliding mode, Phys. Fluids **31**, 051904 (2019).

[27] R. J. Bomphrey, T. Nakata, P. Henningsson, and H.-T. Lin, Flight of the dragonflies and damselflies, Philos. Trans. R. Soc. B **371**, 20150389 (2016).

[28] B. Newman, S. Savage, and D. Schouella, *Model Tests on a Wing Section of an* Aeschna *dragonfly, in Scale Effects in Animal Locomotion*, edited by T. J. Pedley (Academic Press, San Diego, CA, 1977).

[29] J. Wakeling, Dragonfly aerodynamics and unsteady mechanisms: A review, Odonatologica **22**, 319 (1993).

[30] A. B. Kesel, Aerodynamic characteristics of dragonfly wing sections compared with technical aerofoils, J. Exp. Biol. **203**, 3125 (2000).

[31] C. J. Rees, Aerodynamic properties of an insect wing section and a smooth aerofoil compared, Nature (London) **258**, 141 (1975).

[32] A. Obata and S. Sinohara, Flow visualization study of the aerodynamics of modeled dragonfly wings, AIAA J. **47**, 3043 (2009).

[33] Y. S. Baik, L. P. Bernal, K. Granlund, and M. V. Ol, Unsteady force generation and vortex dynamics of pitching and plunging aerofoils, J. Fluid Mech. **709**, 37 (2012).

[34] D. E. Rival, J. Kriegseis, P. Schaub, A. Widmann, and C. Tropea, Characteristic length scales for vortex detachment on plunging profiles with varying leading-edge geometry, Exp. Fluids **55**, 1660 (2014).

[35] Y. Fujita and M. Iima, Aerodynamic performance of dragonfly wing model that starts impulsively: How vortex motion works, J. Fluid Sci. Technol. **18**, JFST0013 (2023).

[36] A. Widmann and C. Tropea, Parameters influencing vortex growth and detachment on unsteady aerodynamic profiles, J. Fluid Mech. **773**, 432 (2015).

[37] G. Luo and M. Sun, The effects of corrugation and wing planform on the aerodynamic force production of sweeping model insect wings, Acta Mech. Sin. **21**, 531 (2005).

[38] L. D. Landau and E. M. Lifshitz, *Fluid Mechanics: Landau and Lifshitz: Course of Theoretical Physics* (Elsevier, Amsterdam, 2013), Vol. 6.

[39] S. Childress, *Mechanics of Swimming and Flying* (Cambridge University Press, Cambridge, UK, 1981), Vol. 2.

[40] G. Rüppell, Kinematic analysis of symmetrical flight manoeuvres of Odonata, J. Exp. Biol. **144**, 13 (1989).

[41] Z. J. Wang, The role of drag in insect hovering, J. Exp. Biol. **207**, 4147 (2004).

[42] M. J. Ringuette, M. Milano, and M. Gharib, Role of the tip vortex in the force generation of low-aspect-ratio normal flat plates, J. Fluid Mech. **581**, 453 (2007).

[43] D. Kim and M. Gharib, Flexibility effects on vortex formation of translating plates, J. Fluid Mech. **677**, 255 (2011).

[44] T. Jardin, J. Choi, and T. Colonius, An empirical correlation between lift and the properties of leading-edge vortices, Theor. Comput. Fluid Dyn. **35**, 437 (2021).

[45] G. E. Karniadakis, G. Karniadakis, and S. Sherwin, *Spectral/hp Element Methods for Computational Fluid Dynamics* (Oxford University Press on Demand, 2005).

[46] H. M. Blackburn, D. Lee, T. Albrecht, and J. Singh, Semtex: A spectral element-Fourier solver for the incompressible Navier-Stokes equations in cylindrical or Cartesian coordinates, Comput. Phys. Commun. **245**, 106804 (2019).

[47] S. Dong, G. E. Karniadakis, and C. Chryssostomidis, A robust and accurate outflow boundary condition for incompressible flow simulations on severely-truncated unbounded domains, J. Comput. Phys. **261**, 83 (2014).

[48] B. Dean and B. Bhushan, Shark-skin surfaces for fluid-drag reduction in turbulent flow: A review, Philos. Trans. R. Soc. A **368**, 4775 (2010).